Data science and AI-I

[9-C-01] Application of Variational Data Assimilation to High-Speed Outflow Boundary-Value Problems of the Ideal Magnetohydrodynamics Equations

*Jose Henrique Arnal[1], Clinton P. T. Groth[1] (1. University of Toronto Institute for Aerospace Studies)

Keywords: Data Assimilation, Magnetohydrodynamics, Adjoint Method, Space Weather

Application of Variational Data Assimilation to High-Speed Outflow Boundary-Value Problems of the Ideal Magnetohydrodynamics Equations

J. H. Arnal and C. P. T. Groth

Corresponding author: `jose.arnal@mail.utoronto.ca`

University of Toronto Institute for Aerospace Studies, Toronto, Canada

Abstract:
Over the last several decades, considerable effort has been dedicated to the computational modelling of space plasmas flows, with applications to heliospheric physics, the solar wind, and space weather science and forecasting. The space weather forecast models that have resulted from this effort are usually based on the equations of ideal magnetohydrodynamics (MHD), an extension of conventional fluid dynamic descriptions to electrically conducting fluids. Despite the sophistication of these techniques, their accuracy in practice is very often limited by uncertainties in model input parameters. The application of data assimilation techniques in which observational measurements are incorporated to constrain model uncertainties offers a means of improving the predictions of global MHD models. To this end, this study presents the first application of a variational-based data assimilation strategy to boundary value problems for the three-dimensional ideal MHD equations, with a systematic treatment for the solenoidal constraint associated with the magnetic field. In the proposed approach, synthetic in-situ data for prototypical steady high-speed MHD outflows representative of the solar wind are considered and model-data mismatch is efficiently minimized via an optimization procedure that makes use of a discrete adjoint method in the evaluation of model parameter gradients. Details of the finite-volume solution method for the ideal MHD equations as well as the data assimilation algorithm for the inner boundary data of the MHD outflows are provided. Additionally, a number of observing system simulation experiments are presented, demonstrating the error-reduction capabilities of the proposed variational data assimilation framework.

Keywords: MHD, Data Assimilation, Adjoint Method, Finite-Volume Method

1   Introduction

Over the last several decades, considerable effort has been dedicated to the computational modelling of space plasmas flows, with applications to heliospheric physics, the solar wind, and space weather science and forecasting. The space weather forecast models that have resulted from this effort are usually based on the equations of ideal magnetohydrodynamics (MHD), an extension of conventional fluid dynamic descriptions to electrically conducting fluids, make use of accurate and robust discretization methods for plasma flows with shocks, automatic mesh refinement, and impose boundary conditions derived from magnetic field measurements of the solar surface [1, 2, 3]. Despite these research efforts, as well as the high level of sophistication and demonstrated efficacy of the resulting space weather forecasting tools, the predictive potential of global MHD-based models are currently not fully realized. In particular, space weather forecasts often fail to match accurately measurements and/or observations. This is largely due to poorly known values for a range of model input parameters. Suspected important sources of the forecast uncertainty include relatively large uncertainties in initial conditions, boundary data, and various sub-physics model parameters. It is noted that modern atmospheric weather and climate forecasts do not however rely solely on accurate numerical models and solution methods alone. They also make extensive use of data assimilation techniques, which combine real-time measurements and observational data from various sources with the predictions of the simulation models, effectively using the observational data to constrain the model predictions, so as to achieve more accurate and reliable forecasts. In contrast, the space weather forecasting community has only just begun to explore the full potential of data assimilation [4, 5, 6].

With this brief review in mind, the present study considers the first application of a variational-based data assimilation strategy to high-speed outflow boundary value problems for the three-dimensional

ideal MHD equations, with a systematic treatment for the solenoidal constraint associated with the magnetic field. The study examines the correction of inner boundary-conditions via variational data assimilation in steady high-speed MHD outflows. This class of flows are prototypical for many space-physics phenomena. Moreover, owing to the super-Alfvénic nature of the flow, the inner boundary data is of particular interest as it fully dictates the plasma properties everywhere within the domain. Synthetic in-situ data is considered for the boundary value problems of interest and model-data mismatch is efficiently minimized via an optimization procedure that makes use of a discrete adjoint method in the evaluation of model parameter gradients.

The organization of the remainder of this short article is as follows. Section 2 presents and summarizes the governing ideal MHD equations of interest. Section 3 then describes the upwind finite-volume spatial discretization and time-marching scheme used to construct numerical approximations to unsteady solutions of the ideal MHD equations in three-dimensional domains. A variational data assimilation strategy for high-speed outflow boundary-value problems is then described in Section 4. This is followed in Section 5 by a summary of the discrete adjoint equations used to compute derivatives associated with the variational data assimilation approach and numerical discretization strategies. Section 6 presents a number of numerical data assimilation experiments with different observation system configurations. Finally, Section 7 provides conclusions and recommendations for future research.

2 Ideal Magnetohydrodynamics Equations

The equations of ideal MHD describe the dynamics of a perfectly electrically conducting inviscid plasma where ion and electron species are treated as a fully-ionized, quasi-neutral, single fluid in thermal equilibrium. These equations may be viewed as an extension of the Euler equations of gas dynamics that accounts for electro-magnetic forces described by Maxwell's equations. In their non-dimensional, weak-conservation form, the ideal MHD equations are a coupled hyperbolic system of non-linear partial differential equations that may be written as

$$\frac{\partial \boldsymbol{U}}{\partial t} + \nabla \cdot \vec{\boldsymbol{F}} = \boldsymbol{S} \,, \tag{1}$$

together with Gauss' law for magnetism given by,

$$\nabla \cdot \vec{B} = 0 \,, \tag{2}$$

where $\boldsymbol{U}$ is the conserved variable solution vector, $\vec{\boldsymbol{F}}$ is the solution flux dyad, $\vec{B} = [B_x, B_y, B_z]^\intercal$ is the magnetic field, and $\boldsymbol{S}$ is a source term that ensures Galilean invariance and is proportional to $\nabla \cdot \vec{B}$. The conserved variable solution vector is given by

$$\boldsymbol{U} = [\rho, \rho\vec{u}, \vec{B}, E]^\intercal \,, \tag{3}$$

where ρ is the plasma density, $\vec{u} = [u_x, u_y, u_z]^\intercal$ is the velocity field, and E is the total energy. The flux dyad, $\vec{\boldsymbol{F}}$, is given by

$$\vec{\boldsymbol{F}} = \begin{bmatrix} \rho\vec{u} \\ \rho\vec{u}\vec{u} - \vec{B}\vec{B} + (p + \frac{\vec{B}\cdot\vec{B}}{2})\vec{\vec{I}} \\ \vec{B}\vec{u} - \vec{u}\vec{B} \\ \vec{u}(E + p + \frac{\vec{B}\cdot\vec{B}}{2}) - \vec{B}(\vec{u}\cdot\vec{B}) \end{bmatrix} \,, \tag{4}$$

where p is the plasma thermal pressure and $\vec{\vec{I}}$ is the identity dyad. A polytropic (thermally and calorically perfect) approximation is assumed for describing the thermodynamic behaviour of the plasma and thus the total energy and plasma pressure are related according to

$$E = \frac{p}{\gamma - 1} + \frac{\rho\vec{u}\cdot\vec{u}}{2} + \frac{\vec{B}\cdot\vec{B}}{2} \,, \tag{5}$$

where γ is the corresponding assumed constant ratio of specific heat capacities. The ideal gas equation of state, $T = \gamma p/\rho$, is also assumed, where T is the non-dimensional plasma temperature. The source vector is given by

$$\boldsymbol{S} = (\nabla \cdot \vec{B})\hat{\boldsymbol{S}} \,, \tag{6}$$

with

$$\hat{\boldsymbol{S}} = -[0, \vec{B}, \vec{u}, \vec{u} \cdot \vec{B}]^{\mathsf{T}}.\tag{7}$$

In the continuous setting, $\boldsymbol{S}$ is exactly equal to zero. However, discretizations of ideal MHD equations do not generally maintain $\nabla \cdot \vec{B} = 0$ because the discrete divergence of the discrete curl is not identically zero. It is therefore often advantageous to keep the source term in order to remove via transport any non-zero $\nabla \cdot \vec{B}$ errors introduced through numerical discretization [7, 8, 9].

3 MUSCL-Type Finite-Volume Method for Ideal MHD

A second-order, MUSCL-type, finite-volume scheme [10] is considered for the numerical solution of the ideal MHD equations. Application of this upwind spatial discretization procedure to the governing equations for a single hexahedral computational cell results in the following semi-discrete form

$$\frac{d\boldsymbol{U}_{\mathcal{I}}}{dt} = -\frac{1}{V_{\mathcal{I}}} \sum_{f=1}^{6} (\vec{\boldsymbol{\mathcal{F}}} \cdot \hat{n} A)_{\mathcal{I},f} - (\vec{B} \cdot \hat{n} A)_{\mathcal{I},f} \hat{\boldsymbol{S}}_{\mathcal{I}} \triangleq \boldsymbol{R}_{\mathcal{I}},\tag{8}$$

where the summation is over the six faces of the $\mathcal{I} \triangleq (i, j, k)$ hexahedral cell, $\boldsymbol{U}_{\mathcal{I}}$ is the cell-averaged values of the solution within cell $\mathcal{I}$, $V_{\mathcal{I}}$ is the cell volume, $\vec{\boldsymbol{\mathcal{F}}}$ is the upwind value of the solution fluxes evaluated at midpoint of a cell interface, and $\hat{n}$ and A are the cell face unit outward normal vector and area respectively. The right-hand side of Eq. (8) is defined as the steady residual, $\boldsymbol{R}_{\mathcal{I}}$. The numerical fluxes are evaluated via the approximate solution of Riemann problems defined in terms of the primitive solution values, $\boldsymbol{W} = [\rho, \vec{u}, \vec{B}, p]^{\mathsf{T}}$, on each side of a hexahedral cell face interface via the Harten-Lax-van Leer-Einfeldt (HLLE) [11] approximate Riemann solver. Second-order spatial accuracy is achieved via piece-wise limited linear reconstruction of the primitive solution vector, resulting in the following assumed form for the primitive solution vector within the $\mathcal{I}$'th computational cell

$$\boldsymbol{W}(\vec{x}_{\mathcal{J}}) = \boldsymbol{W}_{\mathcal{I}} + \boldsymbol{\phi}_{\mathcal{I}} \circ \boldsymbol{G}_{\mathcal{I}}^{\mathsf{T}} \Delta \vec{x}_{\mathcal{J}\mathcal{I}}\tag{9}$$

where $\boldsymbol{\phi}_{\mathcal{I}}$, is a slope limiter, and $\boldsymbol{G}_{\mathcal{I}}$ is an approximation of the primitive solution gradient, $\partial \boldsymbol{W}/\partial \vec{x}$, evaluated at the $\mathcal{I}$'th computational cell. In addition, $\Delta(\cdot)_{\mathcal{J}\mathcal{I}}$ denotes the difference operator defined by $\Delta(\cdot)_{\mathcal{J}\mathcal{I}} = (\cdot)_{\mathcal{J}} - (\cdot)_{\mathcal{I}}$. The method of least-squares [12] is used here to specify $\boldsymbol{G}$. With this approach, the gradient, $\vec{g}$, corresponding to each element, w, of the primitive solution vector is determined by the solution of the following linear system

$$\Delta \boldsymbol{X}_{\mathcal{I}}^{2} \vec{g}_{\mathcal{I}} = \Delta \boldsymbol{X} \Delta \boldsymbol{w}_{\mathcal{I}},\tag{10}$$

where the left hand side matrix is given by

$$\Delta \boldsymbol{X}_{\mathcal{I}}^{2} = \sum_{\mathcal{K} \in \mathcal{S}_{\mathcal{I}}} \Delta \vec{x}_{\mathcal{K}\mathcal{I}} \Delta \vec{x}_{\mathcal{K}\mathcal{I}}^{\mathsf{T}},\tag{11}$$

and the right hand side vector is given by

$$\Delta \boldsymbol{X} \Delta \boldsymbol{w}_{\mathcal{I}} = \sum_{\mathcal{K} \in \mathcal{S}_{\mathcal{I}}} \Delta \vec{x}_{\mathcal{K}\mathcal{I}} \Delta w_{\mathcal{K}\mathcal{I}},\tag{12}$$

where $\mathcal{S}_{\mathcal{I}}$ is the reconstruction stencil, taken to include neighbouring cells that share a face, edge, or corner with the cell of interest, and is therefore given by

$$\mathcal{S}_{\mathcal{I}} = \{(l, m, n) | l = i + [-1, 0, 1], \, m = j + [-1, 0, 1], \, n = k + [-1, 0, 1]\}.\tag{13}$$

For the unsteady initial-boundary-value problems of interest here, the semi-discrete form of the ideal MHD equations is solved by adopting a method-of-lines approach and applying a Runge-Kutta time-marching scheme. Second-order temporal accuracy is achieved by using a strong stability preserving

(SSP), second-order, Runge-Kutta, time-marching scheme [13, 14] given by

$$\widetilde{U}^{n+1} = U^n + \Delta t R(U^n) \,, \tag{14}$$

$$U^{n+1} = \frac{1}{2}(U^n + \widetilde{U}^{n+1} + \Delta t R(\widetilde{U}^{n+1})) \,, \tag{15}$$

where U^n stores the cell-averaged conserved solution vectors for the entire grid at the nth time step. The SSP time-marching scheme ensures monotone solutions for an appropriately restrictive choice of the global time step, Δt, satisfying the usual Courant-Friedrichs-Lewy criteria [15]. Similar to the steady residual, R, the unsteady residual, $\tilde{R}$, can be defined by rearranging Eqs. (14) and (15), to yield

$$\tilde{R} \triangleq \frac{U^{n+1} - U^n}{\Delta t} - \frac{R(U^n) + R(\widetilde{U}^{n+1})}{2} = 0 \,. \tag{16}$$

4 Variational Data Assimilation

The assimilation of *in situ* observational measurements is now considered in the context of supersonic and super-Alfvénic plasma outflow between concentric spheres. Despite its unusual specificity, this type of flow is of particular interest due to its similarity with the solar wind. The main objective is to combine the outputs of numerical ideal MHD solutions with sparse observational data to obtain optimal estimate of plasma properties while accounting for uncertainties in both the observational measurements and the model parameters.

In the protoypical setting of super-Alfvénic plasma outflow studied herein, the inner Derichlet boundary conditions fully dictate the plasma properties everywhere in the spatial domain save for an initial transient that is also dependant on initial conditions. The data assimilation strategy taken here is therefore solely focused on the estimation of inner boundary conditions. A so-called strong-constraint variational data assimilation approach is adopted where the ideal MHD upwind finite-volume model is assumed perfect, and model-data errors are driven entirely by errors in the boundary conditions and in the observational data. Following a standard data assimilation approach, all error statistics are assumed to be Gaussian. More precisely, the unknown inner boundary values, $U_{\partial\Omega}$, are assumed to be of the form given by

$$U_{\partial\Omega} = U_{\partial\Omega}^{\text{truth}} + \zeta \,, \tag{17}$$

where $U_{\partial\Omega}^{\text{truth}}$ is the true boundary condition, and ζ is an error term corresponding to a random sample of a multivariate Gaussian distribution with zero mean and known covariance, $\Sigma_{\partial\Omega}$. The observational data, d, is also assumed to take a similar form given by

$$d = \mathcal{H}(U^{\text{truth}}) + \xi \,, \tag{18}$$

where U^{truth} is the true solution vector, $\mathcal{H}$ is an operator that maps the solution space to the observations space, and ξ is a Gaussian error term with zero mean and known covariance, Σ_d. With these assumptions, it may be shown than the minimum variance estimate of the boundary conditions is given by the solution of the following minimization problem

$$
\begin{aligned}
\min_{U_{\partial\Omega}} \quad & J = \frac{1}{2}||U_{\partial\Omega} - \hat{U}_{\partial\Omega}||^2_{\Sigma_{\partial\Omega}^{-1}} + \frac{1}{2}\sum_{n=1}^{N}||\mathcal{H}(U^n) - d^n||^2_{\Sigma_d^{-1}} \,, \\
\text{s.t.} \quad & \tilde{R} = 0 \,,
\end{aligned}
\tag{19}
$$

where $\hat{U}_{\partial\Omega}$ denotes the *a priori* estimate of $U_{\partial\Omega}$, and N is the total number of time steps. The information contained in the observational data can therefore be effectively assimilated into the ideal MHD model by numerically solving this large optimization problem.

5 Discrete Adjoint Equations

The constrained minimization problem of Eq. (19) can more readily be solved by casting it as an *unconstrained* problem through straightforward application of the method of Lagrange multipliers. Adopting

this approach, the lagrangian, $\mathcal{L}$, is given by

$$\mathcal{L} = J + \sum_{n=0}^{N-1} (\boldsymbol{\lambda}^{n+1})^{\mathsf{T}} \tilde{\boldsymbol{R}}(\boldsymbol{U}^{n+1}, \boldsymbol{U}^n), \tag{20}$$

where the Lagrange multiplier, $\boldsymbol{\lambda}$, is introduced. It is noted that Lagrange multipliers are often also refered to as adjoint variables in the PDE constrained optimization literature—this convention is also adopted herein.

Eq. (20) can effectively be minimized through gradient based numerical optimization techniques. The gradient of $\mathcal{L}$ can be obtained by first setting the derivatives of $\mathcal{L}$ with respect to the adjoint variables to zero, yielding

$$\tilde{\boldsymbol{R}}(\boldsymbol{U}^{n+1}, \boldsymbol{U}^n) = \boldsymbol{0} \tag{21}$$

which recovers the original discrete ideal MHD constraint. Similarly, differentiating with respect to the solution vector, and setting the result to zero, yields

$$\boldsymbol{\lambda}^n = \left[\frac{\partial \boldsymbol{\mathcal{M}}^n}{\partial \boldsymbol{U}^n}\right]^{\mathsf{T}} \boldsymbol{\lambda}^{n+1} - \left[\frac{\partial \boldsymbol{\mathcal{H}}(\boldsymbol{U}^n)}{\partial \boldsymbol{U}^n}\right]^{\mathsf{T}} \Sigma_{\boldsymbol{d}}^{-1} (\boldsymbol{\mathcal{H}}(\boldsymbol{U}^n) - \boldsymbol{d}^n), \tag{22}$$

where, without loss of generality, $\tilde{\boldsymbol{R}}$ is writen as $\tilde{\boldsymbol{R}}(\boldsymbol{U}^{n+1}, \boldsymbol{U}^n) = \boldsymbol{U}^{n+1} - \boldsymbol{\mathcal{M}}(\boldsymbol{U}^n)$. Eq. (22) may be interpreted as the backwards in time temporal evolution of the adjoint variables. Finally, differentiating with respect to the boundary conditions gives

$$\frac{\partial \mathcal{L}}{\partial \boldsymbol{U}_{\partial \Omega}} = \boldsymbol{\Sigma}_{\boldsymbol{U}_{\partial \Omega}}^{-1} (\boldsymbol{U}_{\partial \Omega} - \hat{\boldsymbol{U}}_{\partial \Omega}) - \sum_{n=1}^{N} \left[\frac{\partial \boldsymbol{\mathcal{M}}^n}{\partial \boldsymbol{U}_{\partial \Omega}}\right]^{\mathsf{T}} \boldsymbol{\lambda}^{n+1}. \tag{23}$$

To fully specify $\partial \mathcal{L}/\partial \boldsymbol{U}_{\partial \Omega}$, the temporal and spatial disctretization strategies employed in the numerical MHD model must also be differentiated. Begining with time discretization, differentiating the time-marching scheme of Eqs. (14)–(15) results in predictor-corrector stages for the adjoint variables given by

$$\widetilde{\boldsymbol{\lambda}}^n = \boldsymbol{\lambda}^{n+1} + \Delta t \left[\frac{\partial \boldsymbol{R}(\widetilde{\boldsymbol{U}}^{n+1})}{\partial \widetilde{\boldsymbol{U}}^{n+1}}\right]^{\mathsf{T}} \boldsymbol{\lambda}^{n+1}, \tag{24}$$

$$\left[\frac{\partial \boldsymbol{\mathcal{M}}^n}{\partial \boldsymbol{U}^n}\right]^{\mathsf{T}} \boldsymbol{\lambda}^{n+1} = \frac{1}{2}\left(\boldsymbol{\lambda}^{n+1} + \widetilde{\boldsymbol{\lambda}}^n + \Delta t \left[\frac{\partial \boldsymbol{R}(\boldsymbol{U}^n)}{\partial \boldsymbol{U}^n}\right]^{\mathsf{T}} \widetilde{\boldsymbol{\lambda}}^n\right). \tag{25}$$

Furthemore, individual elements of the jacobian-transpose-vecotor product, $\hat{\boldsymbol{\lambda}} = [\partial \boldsymbol{R}/\partial \boldsymbol{U}]^{\mathsf{T}} \boldsymbol{\lambda}$, associated with the upwind finite-volume discretization strategy are given by

$$\hat{\boldsymbol{\lambda}}_{\mathcal{I}} = \sum_{d=1}^{3} \sum_{\mathcal{J} \in \mathcal{S}_d} A_{\mathcal{J}} \left[\frac{\partial ((\vec{\boldsymbol{\mathcal{F}}} \cdot \hat{n})_{\mathcal{J}} - (\vec{B} \cdot \hat{n})_{\mathcal{J}} \hat{\boldsymbol{S}}_{\mathcal{I}})}{\partial \boldsymbol{U}_{\mathcal{I}}}\right]^{\mathsf{T}} \Delta_{\mathcal{J}} \frac{\boldsymbol{\lambda}_{\mathcal{I}}}{V_{\mathcal{J}}}, \tag{26}$$

where the stencils, $\mathcal{S}_1, \mathcal{S}_2, \mathcal{S}_3$, are defined as

$$\mathcal{S}_1 \triangleq \left\{(l, m, n) \mid l = i + [\frac{-3}{2}, \frac{-1}{2}, \frac{1}{2}, \frac{3}{2}], m = j + [-1, 0, 1], n = k + [-1, 0, 1]\right\}, \tag{27}$$

$$\mathcal{S}_2 \triangleq \left\{(l, m, n) \mid l = i + [-1, 0, 1], m = j + [\frac{-3}{2}, \frac{-1}{2}, \frac{1}{2}, \frac{3}{2}], n = k + [-1, 0, 1]\right\}, \tag{28}$$

$$\mathcal{S}_3 \triangleq \left\{(l, m, n) \mid l = i + [-1, 0, 1], m = j + [-1, 0, 1], n = k + [\frac{-3}{2}, \frac{-1}{2}, \frac{1}{2}, \frac{3}{2}]\right\}, \tag{29}$$

and $\Delta_{\mathcal{J}}$ is defined as a difference operator of the right and left values of the $\mathcal{J}$'th cell interface. The derivatives of the numerical flux function, $\vec{\boldsymbol{\mathcal{F}}}$, are obtained by direct differentiation of the HLLE aproximate Riemann solver and the least-squares reconstruction scheme of Eqs. (9)–(10).
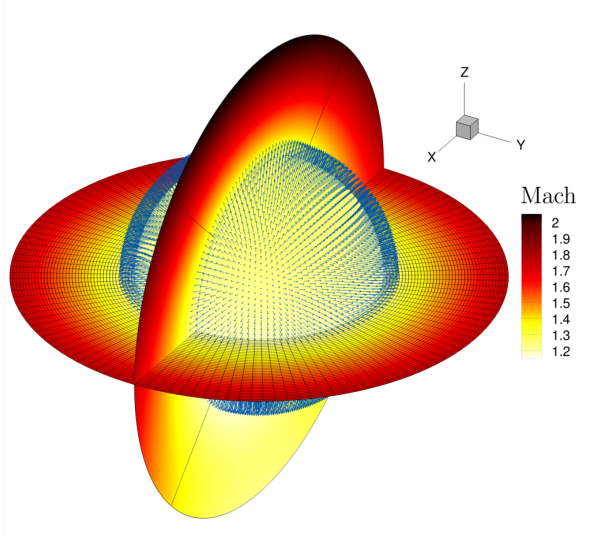
Figure 1: Exact Mach number distribution of the manufactured solution in the inner boundary, x-y plane, and z-x plane, with magnetic field lines on the inner boundary indicated by blue arrows.

6   Numerical Experiments

As described in Section 4, this study considers the application of variational data assimilation to supersonic and super-Alfvénic plasma outflow between concentric spheres. In particular, the manufactured solution of Ivan *et al.*[16] is examined. This ideal MHD problem consists of a steady-state axi-symmetric exact solution of magnetized gas flowing outward at supersonic and super-Alfvénic speeds with primitive quantities given by

$$\boldsymbol{W}(x,y,z) = \left[r^{-\frac{5}{2}} , \frac{x}{\sqrt{r}} , \frac{y}{\sqrt{r}} , \frac{z}{\sqrt{r}} + kr^{\frac{5}{2}} , \frac{x}{r^3} , \frac{y}{r^3} , \frac{z}{r^3} + k , r^{-\frac{5}{2}} \right]^{\mathsf{T}} , \tag{30}$$

where r is the radial distance and $k = 0.017$. The Mach number distribution associated with this solution is shown in Fig. (1).

In accordance with the method of manufactured solutions, a volumetric source term, $\boldsymbol{Q}$, must be added to the right-hand side of Eq. (1) to balance the non-analytical solution. For the solution given in Eq. (30), the additional source term is given by

$$\boldsymbol{Q} = \begin{bmatrix} 0 \\ \frac{1}{2}xr^{-\frac{5}{2}}(r^{-1} - 5r^{-2} - kz) \\ \frac{1}{2}yr^{-\frac{5}{2}}(r^{-1} - 5r^{-2} - kz) \\ \frac{1}{2}zr^{-\frac{5}{2}}(r^{-1} - 5r^{-2} - kz) + \frac{5}{2}r^{-\frac{1}{2}}k(1 + krz) + kr^{-\frac{1}{2}} \\ \vec{0} \\ \frac{1}{2} + kz(3.5r^{-1} + 2kz) + \frac{(kr)^2}{2}(7 + 5krz) \end{bmatrix} , \tag{31}$$

assuming an adiabatic index of $\gamma = 1.4$.

In order to assess the proposed variational data assimilation strategy, a perturbation to the exact inner boundary conditions is added to simulate errors arising from uncertainties in the inner boundary. The perturbation, $\boldsymbol{\zeta}$, corresponds to a bump function added to each of the primitive variables and is given by

$$\boldsymbol{\zeta}(x,y,z) = \frac{1}{2}\exp\left(-3\arcsin\left(\frac{\sqrt{(x - R_0)^2 + y^2 + 4z^2}}{2r} \right) \right)\boldsymbol{W}_{\partial\Omega} , \tag{32}$$

where R_0 is the radial distance of the inner boundary. The perturbation corresponding to the density field is illustrated in Fig. (2).

With the additional perturbations, the problem is simulated in an unsteady fashion with errors propagating from the inner boundary to the rest of the three-dimensional solution domain. The exact, unperturbed, solution is used as the initial conditions to allow for time accurate calculations. Once steady state is reached, however, the solution is fully determined by the inner boundary conditions. The
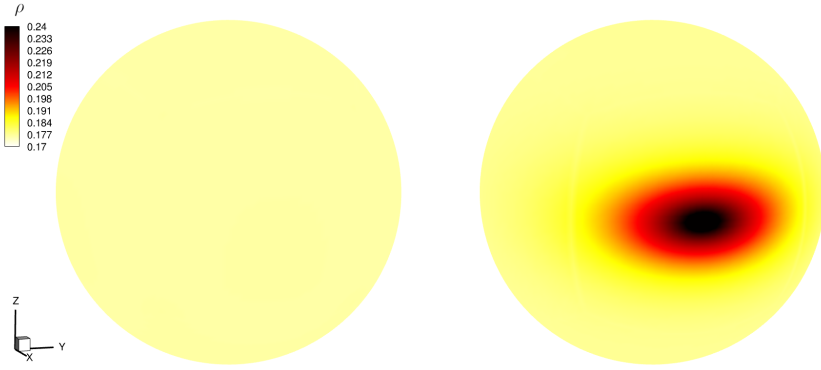
Figure 2: Comparison between the exact (left) and perturbed (right) density inner boundary-conditions for the numerical data assimilation experiments.

solution obtained by imposing the erroneous boundary conditions is denoted as the 'background' solution as it represents the best estimate of the solution prior to any corrections from data assimilation. A computational mesh consisting of 1,058,400 cells is used with inner and outer spheres of radius $R_0 = 2$ and $R_1 = 4$ respectively. Simulations are performed for 1 non-dimensional unit of time, which is sufficiently long for the flow to reach a quasi steady-state. Synthetic observations are generated by sampling the ground-truth, unperturbed, solution along the path of a fictitious spacecraft with an orbital radius of 3 on the x-y plane and with start and end azimuthal angles of $-45°$ and $45°$ respectively. A total of 42 synthetic measurements are taken during the duration of the simulation corresponding to the 42 computational cells from where observations are gathered. Each observation includes all of the eight conserved quantities in the MHD equations.

An implementation of the limited memory Broyden–Fletcher–Goldfarb–Shanno algorithm found in the Adept 2.0 library [17] is used to solve the data assimilation optimization problem of Eq. (19). An inordinately conservative stopping criteria of 100 optimization iterates was imposed to ensure convergence. It is noted however that the majority of the functional minimization occurs in the first 20 iterations. It is also noted that for the preliminary results discussed in this article, the a priori term in Eq. (19) is neglected, and only the model-data mismatch term is taken into consideration. In addition, spatial and temporal accuracy is restricted here to first-order accuracy as a first step. The inclusion of a priori information, as well as the application of second-order accurate discretization schemes, will be the subject of future follow-on studies.

Selected plasma properties evaluated at the fictitious spacecraft's space-time locations are given in Fig. (3) for the ground-truth, background, and data assimilated solutions which demonstrate a near perfect match between the data assimilated and ground truth predictions. Furthermore, the relative error in plasma energy is compared for both the background and data assimilated simulations in Fig. (4). It is evident that although the synthetic observational data is highly sparse, the data assimilation strategy is able to minimize solution errors in a large and three-dimensional extent of the solution domain and thus provides encouraging results for future studies involving more realistic simulations of space physics phenomena. Nevertheless, a neighborhood of high relative error can be seen in Fig. (4c) and Fig. (4d) concentrated in the negative azimuthal region. This high error region is associated with a lack of valuable observations due to the initial transient of the boundary perturbation to the spacecraft orbit radius. Prior to the arrival of boundary information, spacecraft measurements, located near the $-45°$ start point of the spacecraft, provide no means to correct the erroneous boundary conditions and therefore poor data assimilation performance is observed in the aforementioned regions. To further illustrate this point, the data assimilation experiment is repeated with all observations occurring simultaneously at the last time step. In this setting, which is analogous to the assimilation of steady-state observations, all observations can make useful contributions to the estimation problem. The relative error in the plasma energy for this second data assimilation experiment is shown in Fig. (5a) where, compared to Fig. (4d), high error regions are no longer observed. A third and final experiment is conducted where observations are mirrored about the z-y plane and therefore placed in the non-perturbed half of the computational domain. With this observation system, very little useful information is ingested resulting in expectantly poor performance as shown in Fig. (5b).
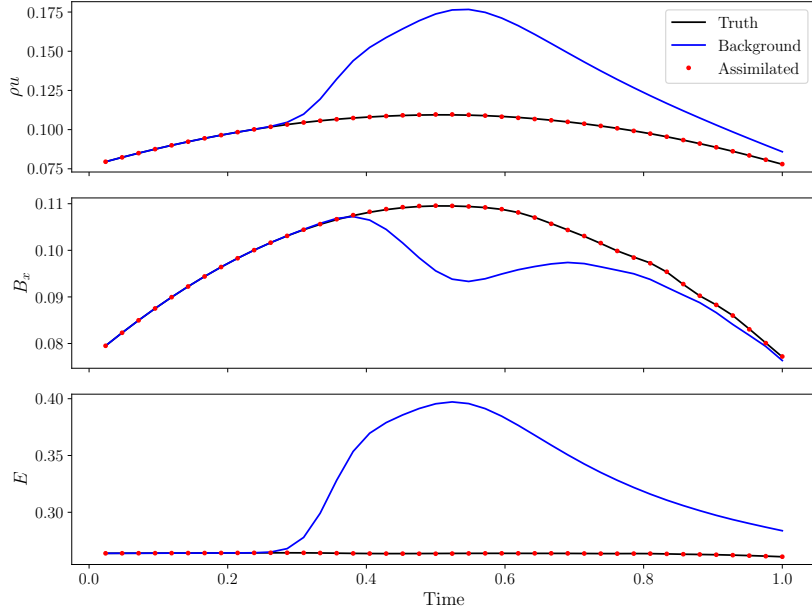
Figure 3: Comparison of predicted plasma $x-$momentum (top), $x-$magnetic field (middle), and energy (bottom) in the ground-truth (black), background (blue), and data assimilated (red) solutions. The spatial location of the solution values correspond to the fictitious observer locations which corresponds to a circular orbit of the x-y plane with a radius of three units from $-45°$ to $45°$ in the azimuthal direction.

7 Conclusions and Future Research

In the present study, a variational data assimilation strategy is proposed to mitigate prediction errors associated with uncertainties in the boundary conditions of high-speed outflow boundary-value problems of fully-ionized plasma flows governed by the ideal MHD equations. These types of flows are ubiquitous in space weather forecasts which is the motivating application of this study. Poorly known inner boundary conditions were successfully corrected by the assimilation of sparse synthetic observations of plasma properties away from the inner boundary. A boundary-value problem constructed with the method of manufactured solutions involving supersonic and super-Alfvénic flow was studied, and the physical and temporal placement of synthetic observations was varied. As expected, greater error reduction was achieved with observations located in error rich regions.

The overall strong performance of the numerical data assimilation experiments provide further motivation to pursue variational data assimilation for space weather applications in future studies. The extension of the strategies outlined in this paper to the practical assimilation of solar wind data is straightforward, with the main challenge laying in appropriately specifying the error covariance of *a priori* boundary data.

(a)

(b)

(c)

(d)
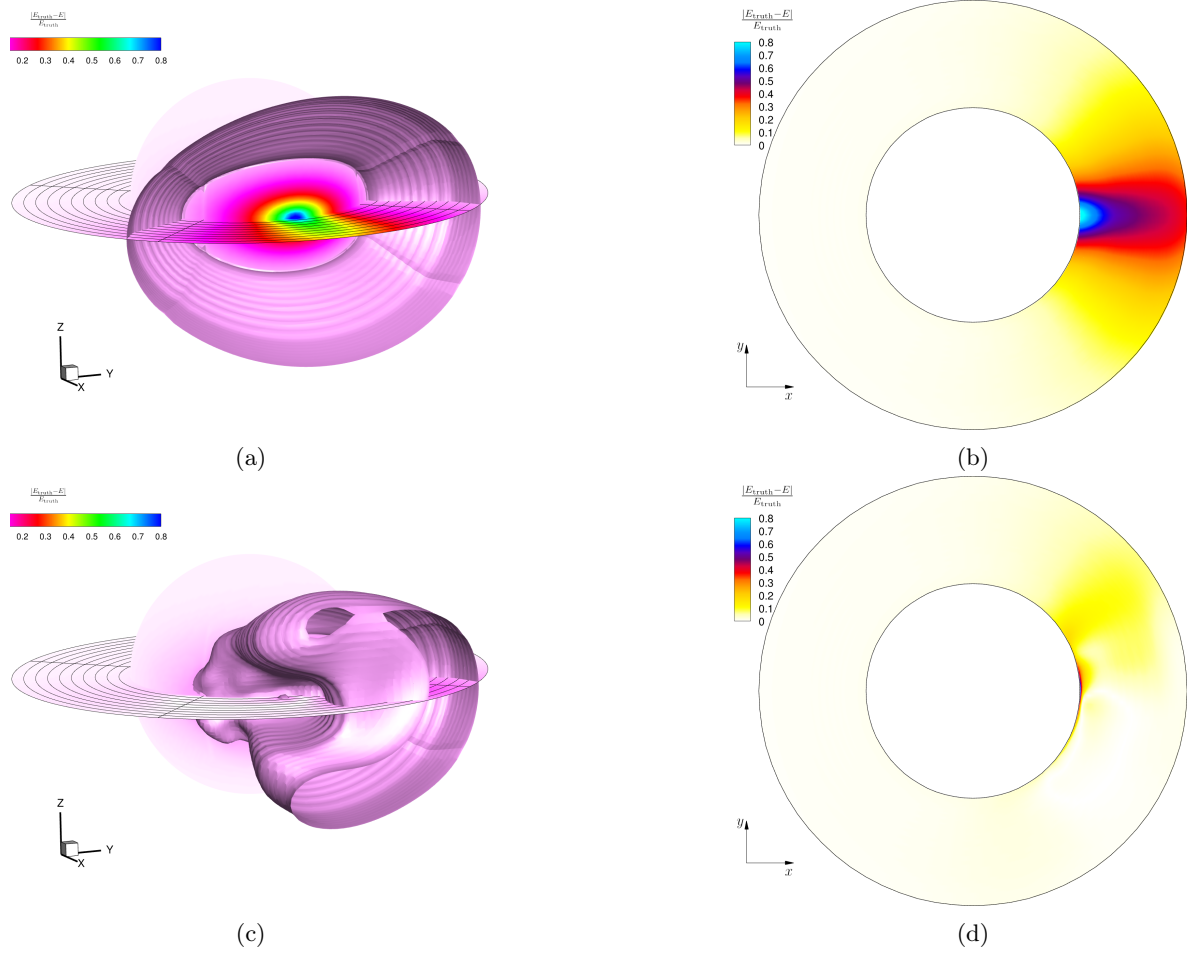
Figure 4: Relative error of plasma energy in the background (top row) and data assimilated (bottom row) predictions. The left column depicts the error on the inner boundary, x-y plane, and along an isosurface 5% relative error. The right column shows the relative error solely on the x-y plane. All quantities are given at a simulation time of $t = 1$.

(a)

(b)
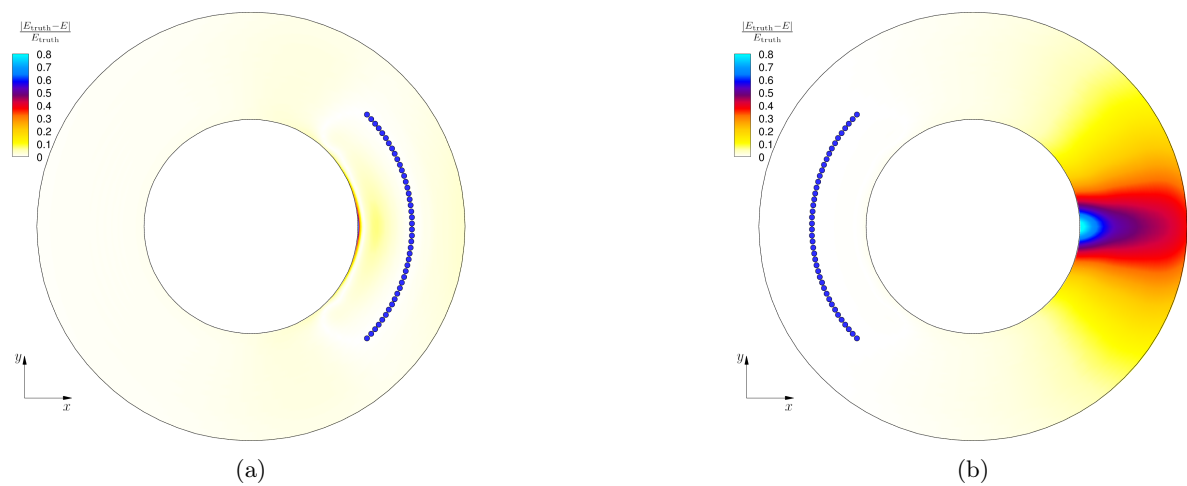
Figure 5: Relative error of plasma energy in the x-y plane corresponding to observation systems with simultaneous observations in the positive (left) and negative (right) x-direction halves of the solution domain. The spatial coordinates of synthetic measurements are denotes by blue circles.

9

References

[1] C. P. T. Groth, D. L. De Zeeuw, T. I. Gombosi, and K. G. Powell. Global three-dimensional MHD simulation of a space weather event: CME formation, interplanetary propagation, and interaction with the magnetosphere. *Journal of Geophysical Research*, 105(A11):25,053–25,078, 2000.

[2] J. Pomoell and S. Poedts. EUHFORIA: European heliospheric forecasting information asset. *Journal of Space Weather and Space Climate*, 8(A35), 2018.

[3] N. M. Narechania, L. Nikolić, L. Freret, H. De Sterck, and C. P. T. Groth. An integrated data-driven solar wind — CME numerical framework for space weather forecasting. *Journal of Space Weather and Space Climate*, 11(8), 2021.

[4] M. Lang and M. J. Owens. A variational approach to data assimilation in the solar wind. *Space Weather*, 17(1):59–83, 2019.

[5] J. H. Arnal, J. Sullivan, and C. P. T. Groth. Variational-based data assimilation of initial value problems for ideal magnetohydrodynamic equations subject to solenoidal constraint. In *Proceedings of the 30th Annual Conference of the CFD Society of Canada (CFD2023), 2023 Joint Congress with Canadian Society for Mechanical Engineering (CSME/CFD2023), Sherbrooke, Quebec, Canada, May 28–31, 2023*, number 258, 2023.

[6] J. H. Arnal and C. P. T. Groth. Quantitative comparison of variational and sequential data assimilation techniques for one-dimensional initial-value problems of ideal MHD. *CompFluids*, 282:106373, 2024.

[7] K. G. Powell. An approximate Riemann solver for magnetohydrodynamics (that works in more than one dimension). Report 94-24, ICASE, July 1994.

[8] K. G. Powell, P. L. Roe, T. J. Linde, T. I. Gombosi, and D. L. De Zeeuw. A solution-adaptive upwind scheme for ideal magnetohydrodynamics. *Journal of Computational Physics*, 154:284–309, 1999.

[9] S. K. Godunov. Symmetric form of the equations for magnetohydrodynamics. Report, Computer Center, Siberian Branch of USSR Academy of Sciences, 1972.

[10] L. Ivan, H. De Sterck, S. A. Northrup, and C. P. T. Groth. Three-dimensional MHD on cubed-sphere grids: Parallel solution-adaptive simulation framework. Paper 2011-3382, AIAA, June 2011.

[11] A. Harten, P. D. Lax, and B. van Leer. On upstream differencing and Godunov-type schemes for hyperbolic conservation laws. *SIAM Review*, 25(1):35–61, 1983.

[12] T. J. Barth and D. C. Jespersen. The design and application of upwind schemes on unstructured meshes. Paper 89-0366, AIAA, January 1989.

[13] C.-W. Shu and S. Osher. Efficient implementation of essentially non-oscillatory shock-capturing schemes. *Journal of Computational Physics*, 77:439–471, 1988.

[14] S. Gottlieb, C.-W. Shu, and E. Tadmor. Strong stability-preserving high-order time discretization methods. *SIAM Review*, 43(1):89–112, 2001.

[15] R. Courant and K. O. Friedrichs. *Supersonic Flow and Shock Waves*. Springer, New York, 5th edition, 1999.

[16] L. Ivan, H. De Sterck, S. A. Northrup, and C. P. T. Groth. Hyperbolic conservation laws on three-dimensional cubed-sphere grids: A parallel solution-adaptive simulation framework. *Journal of Computational Physics*, 255:205–227, 2013.

[17] R. J. Hogan. Adept 2.0: a combined automatic differentiation and array library for C++, 2017.